Applied Geochemistry 139 (2022) 105265

Contents lists available at ScienceDirect

Applied Geochemistry

journal homepage: www.elsevier.com/locate/apgeochem

Density functional theory calculations of nitrogen and oxygen equilibrium isotope fractionations in NO_3^-–NO_2^-–H_2O aqueous system reveal inverse kinetic isotope effects during nitrite oxidation

Yuyang He [a,b,*], Long Li [c]

[a] Key Laboratory of Earth and Planetary Physics, Institute of Geology and Geophysics, Chinese Academy of Sciences, Beijing, China
[b] State Key Laboratory of High Temperature Gas Dynamics, Institute of Mechanics, Chinese Academy of Sciences, Beijing, China
[c] Department of Earth and Atmospheric Sciences, University of Alberta, Edmonton, Alberta, T6G 2E3, Canada

ARTICLE INFO

Editorial Handling by: Dr. Qusheng Jin

Keywords:
Reduced partition function ratio
Nitrate reduction
Water-droplet model
Solvent effect
Inverse kinetic isotope effect

ABSTRACT

Nitrate and nitrite play key roles in the nitrogen cycle on Earth's surface. The isotope fractionation during nitrate reduction on enzymatic level involves multiple steps, including transfer of free NO_3^- to the activate site on nitrate reductase and NO_2^- equilibration with ambient water. However, the isotope fractionation factors of ^{15}N and ^{18}O among NO_3^-, NO_2^-, and H_2O molecules in aqueous phases are poorly constrained. It strongly impedes the understanding of the involved processes and using stable isotopes to quantitatively examine the biogeochemical nitrogen cycle. In this contribution, we employ the density functional theory method with the Urey-Bigeleisen-Goeppert-Mayer model to predict the nitrogen and oxygen equilibrium isotope fractionation factors of NO_3^-, NO_2^-, and H_2O molecules in gaseous and aqueous phases. Our calculation results show that the solvent effect has a large influence on equilibrium isotope fractionation for oxygen in water (+10.1‰ between liquid and vapor water at 25 °C), which is different to the little solvent effects on both oxygen and nitrogen in nitrate and nitrite. The calculated temperature-dependent equilibrium isotope fractionations between nitrogen of NO_3^- and NO_2^-, and oxygen of H_2O and NO_2^- are consistent with previous laboratory experiments. Our results confirm that the oxygen equilibrium isotope fractionations between NO_3^- and NO_2^- should be +9.4‰ at 25 °C. Integrating the new results and previously reported kinetic isotope effects of nitrate reduction, we demonstrate inverse kinetic isotope effects for both nitrogen (+15.4‰) and oxygen (+5.2‰) during nitrite oxidation, which falls in the range of previous experiments. The new results enable us to use both nitrogen and oxygen isotopes as a bonded isotope tool to quantitatively assess the nitrogen cycle in low-temperature environments.

1. Introduction

Nitrate is a key component in global nitrogen cycle and the major source of biologically available nitrogen. Quantitative assessment of nitrate reduction (NR), which is the initial step of denitrification, is crucial to the understanding of the biological nitrogen cycling processes in natural environments. The reaction mechanisms of nitrate reduction observed in the field are usually inferred from the change of the nitrogen and oxygen isotope ratios ($^{15}R = {}^{15}N/{}^{14}N$ and $^{18}R = {}^{18}O/{}^{16}O$) of nitrate (e.g., Sigman et al., 2005; Granger et al., 2008; Casciotti et al., 2013; Wankel et al., 2015).

If a reaction reaches equilibrium, the isotope composition difference between the reactant and product is referred to as equilibrium isotope effect (EIE). It can be expressed as $EIE = {}^{H}K/{}^{L}K$, where K denotes the equilibrium constant of the reaction, H denotes heavy isotope (also the common isotope in nitrogen or oxygen), and L denotes light isotope (also the rare isotope in nitrogen or oxygen), or $EIE = \beta_{product}/\beta_{reactant}$, where the β factor (aka the reduced partition function ratio) refers to the equilibrium isotope fractionation factor between an atom in a specific bond environment and its atomic form (Urey, 1947; Bigeleisen and Goeppert Mayer, 1947; Bao et al., 2015; He et al., 2020b). If a reaction is uni-directional, its kinetic isotope effect (KIE) can be considered as the EIE of its transition state and reactant (Jones and Urbauer, 1991; Bao et al., 2015; He et al., 2020b). It can be expressed as $KIE = {}^{H}k/{}^{L}k$, where

Abbreviations: DFT, Density Funcitonal Theory; EIE, Equilibrium Isotope Effect; KIE, Kinetic Isotope Effect; TS, Transition State; NR, Nitrate Reduction; NO, Nitrite Oxidation; IEFPCM, Integral-Equation-Formalism Polarizable Continuum Model.

* Corresponding author. Key Laboratory of Earth and Planetary Physics, Institute of Geology and Geophysics, Chinese Academy of Sciences, Beijing, China.
E-mail addresses: yhe@mail.iggcas.ac.cn (Y. He), long4@ualberta.ca (L. Li).

https://doi.org/10.1016/j.apgeochem.2022.105265
Received 1 November 2021; Received in revised form 1 March 2022; Accepted 6 March 2022
Available online 11 March 2022

k denotes the first-order kinetic constant of an elementary reaction, or $KIE = \beta_{TS}/\beta_{reactant}$, where TS denotes transition state. The EIE value of a reaction equals the ratio of KIE values of forward and backward reactions ($EIE = KIE_f/KIE_b$; Bao et al., 2016; He et al., 2020b). For better illustration, *EIE* and *KIE* values are often reported in forms of ln*EIE* and ln*KIE* values in per mil (‰).

It is commonly assumed that light isotopes react faster than heavy isotopes during a kinetic process, i.e., ${}^{H}k < {}^{L}k$, and thus the *KIE* values for both forward and backward reactions are smaller than 1, which is called a "normal" KIE. If heavy isotopes react faster than light isotopes during a kinetic process, its KIE is considered as an "inverse" one. It should be noted that, Bigeleisen (1949) initially defined KIE in the opposite way ($KIE = {}^{L}k/{}^{H}k$ or $KIE = \beta_{reactant}/\beta_{TS}$), and thus in such case a normal *KIE* value would be greater than 1. In the study of nitrite oxidation (NO), both $KIE = {}^{H}k/{}^{L}k$ (Jacob et al., 2017; Liu et al., 2021) and $KIE = {}^{L}k/{}^{H}k$ (Casciotti, 2009; Buchwald and Casciotti, 2010; Kobayashi et al., 2019; Boshers et al., 2019; Karolewski et al., 2021) have been used. This sometimes causes confusion. To adapt to the tradition of isotope geochemistry and for comparison purposes, we adopted the definition with normal $KIE < 1$ and converted all the *KIE* values in literature accordingly for this study. In such context, negative ln*EIE* and ln*KIE* values mean that the light isotopes tend to be enriched in reactant during a process.

Enzymatic nitrate reduction can be described as multiple elementary steps (Cerqueira et al., 2009, 2015; Sparacino-Watkins et al., 2014; Niks and Hille, 2019): (1) free hydrated NO_3^- occupies the activate site on nitrate reductase and forms an O_2NO-E complex (Fig. 1, k_1, E denotes enzyme). This process can be considered in equilibrium. (2) NO_2^- dissociates from the O_2NO-E complex through a transition state (TS-E complex). The KIEs in both the forward (Fig. 1, k_2) and the backward reactions (Fig. 1, k_3) need to be considered. (3) The oxygen in NO_2^- and on the enzyme, i.e., the O-E complex, are considered in equilibrium with ambient water oxygen (Fig. 1, k_4 and k_5). (4) NO_2^- removes from the reaction site (Fig. 1, k_6). The isotope effect of each step needs to be integrated to obtain the isotope fractionation factor of nitrate reduction.

Nitrate reduction occurs at a molybdenum center of nitrate reductase (Hille, 1996, 2002). Nitrite is also likely oxidized to nitrate at the molybdenum center of nitrite oxidoreductase, which is a membrane-associated iron-sulfur molybdoprotein (Meincke et al., 1992; Spieck et al., 1998). Consequently, the transition state of nitrate reduction can be considered as the approximate transition state of nitrite oxidation. The KIE of nitrite oxidation has been examined by a number of laboratory incubation experiments, from which inverse KIEs have been repeatedly observed. For example, Casciotti (2009) carefully evaluated all possible responsible factors and proposed an inverse nitrogen isotope effect as the explanation based on nitrite oxidation experiments. Later experiments by Buchwald and Casciotti (2010) demonstrated that inverse isotope effects existed in both oxygen and nitrogen during nitrite oxidation. Inverse KIEs have been verified by a number of more recent studies (e.g., Brunner et al., 2013; Jacob et al., 2017; Boshers et al., 2019; Kobayashi et al., 2019; Karolewski et al., 2021; Liu et al., 2021). Given that the KIE of an uni-directional process is rarely inverse in experimental and field studies, these observations need careful evaluation.

Analysis of the β factors of each component in the process at molecular and enzymatic levels can provide important insights to

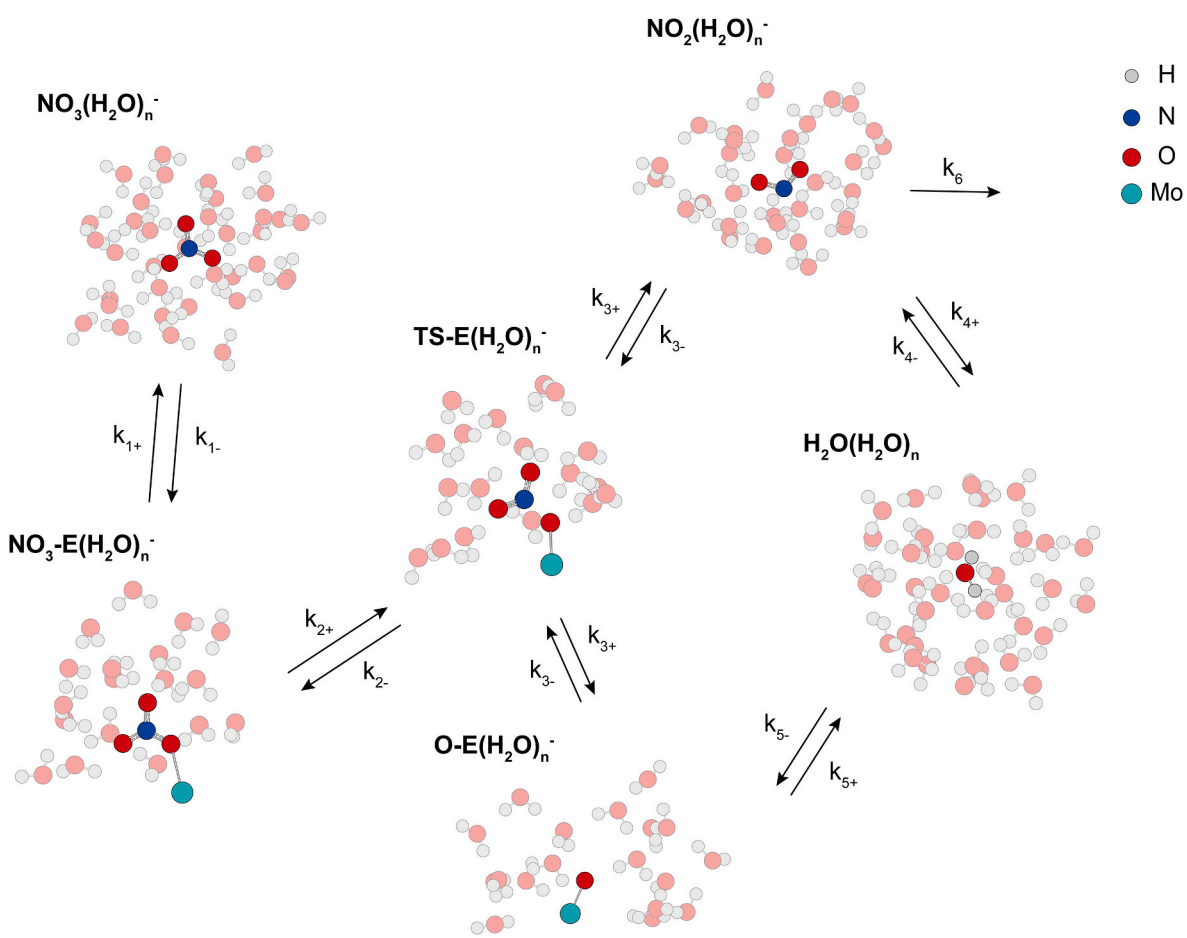

Fig. 1. Schemes of proposed nitrate reduction mechanism by nitrate reductase (modified from Cerqueira et al., 2009, 2015; Sparacino-Watkins et al., 2014; Niks and Hille, 2019). Enzymes are represented by the Mo atom of the active center. Light gray, blue, red, and green spheres represent H, N, O, and Mo atoms, respectively. The *k*s are first-order reaction constants for each elementary step. E denotes enzymes.

understand these process. Density Functional Theory (DFT) method with the Urey-Bigeleisen-Goeppert-Mayer (U–B-GM) model has been demonstrated to be a robust way to determine β factors by our previous work, in which the *KIE* values of the k_2 step was determined based on the β factors of NO_3-E$(H_2O)_n^-$ and TS-E$(H_2O)_n^-$ for *Rhodobacter sphaeroides* NapA nitrate reductase (He et al., 2021). However, the β factors of NO_3^-, NO_2^-, and H_2O molecules in aqueous phases, which are equally crucial for the nitrate-nitrite system, are not yet well constrained.

For N isotopes, previous theoretical calculations show that the $\ln^{15}EIE_{NO_3^- - NO_2^-}$ value is in the range of +54.0‰ to +86.6‰ at 25 °C (Spindel, 1954; Begun and Fletcher, 1960; Stern et al., 1962; Monse et al., 1969; Casciotti, 2009; Walters and Michalski, 2015), which have greater magnitudes than our calculated $\ln^{15}KIE_{NR}$ result (−32.4‰; He et al., 2021). This means that nitrite oxidation is expected to have an inverse $\ln^{15}KIE_{NO}$ value of +20 to +50‰.

Meanwhile, for the O isotopes, two previous theoretical studies have examined the $\ln^{18}EIE_{NO_3^- - NO_2^-}$ values, but gave very different results, i.e., +11.0‰ in Monse et al. (1969) and −1.3‰ in Walters and Michalski (2016) at 25 °C. Based on our previous calculations (He et al., 2021), if the $\ln^{18}EIE_{NO_3^- - NO_2^-}$ value is +11.0‰, nitrite oxidation is expected to be an inverse $\ln^{18}KIE_{NO}$ value of ~+7‰. If the $\ln^{18}EIE_{NO_3^- - NO_2^-}$ value is −1.3‰, where NO_2^- is expected to be more enriched in ^{18}O than NO_3^-, nitrite oxidation is expected to have a normal $\ln^{18}KIE_{NO}$ value of ~−5‰. The inconsistency between Monse et al. (1969) and Walters and Michalski (2016) results in fundamentally different conclusions regarding the KIE of nitrite oxidation, which brings difficulty in the study of nitrate-nitrite reaction complex, and thus needs a thorough reassessment.

One more problem for the study of nitrate-nitrite reaction complex lies in the $^{18}\beta$ value of H_2O. The $^{18}\beta$ value of gaseous H_2O has been calculated on different theoretical levels (Urey, 1947; Saxena et al., 1962; Thornton, 1962; Bottinga, 1968; Richet et al., 1977; Walters and Michalski, 2016), but can hardly be directly compared to the reported $^{18}\beta_{NO_3^-}$ and $^{18}\beta_{NO_2^-}$ values (Monse et al., 1969; Walters and Michalski, 2016). In addition, enzymatic reactions usually occur in aqueous phases. Previous calculated β values of NO_3^- and NO_2^- were mostly determined in gaseous phases (Urey, 1947; Spindel, 1954; Begun and Fletcher, 1960; Saxena et al., 1962; Stern et al., 1962; Thornton, 1962; Bottinga, 1968; Monse et al., 1969; Richet et al., 1977; Casciotti, 2009; Walters and Michalski, 2015, 2016), or with implicit solvent effect (Casciotti, 2009; Walters and Michalski, 2015). Explicit water molecules can induce a significant isotope effect. For instance, at 25 °C, the $\ln^{18}EIE$ values between H_2O and OH^- in aqueous phase diverges from gaseous phase for ~20‰ (Zeebe, 2020); and the $\ln^{15}EIE$ values between ammonia and ammonium in aqueous phase diverges from gaseous phase for 7.9‰ (Li et al., 2021). To fully address the solvent effect, a hybrid-solvent model, which includes both implicit and explicit solvent effects, is needed.

In this study, we performed DFT calculations for NO_3^-, NO_2^-, and H_2O molecules in gaseous phases, by the implicit solvent model and the hybrid-solvent model. Based on the calculation results, we further derive the EIE among NO_3^-, NO_2^-, and H_2O, and the KIE of nitrite oxidation.

2. Methods

2.1. Density functional theory calculations

All geometry optimization and harmonic vibrational frequencies calculations for the ground states are performed in software Gaussian 16 (Frisch et al., 2016). To be consistent and comparable with our previous KIE calculations for nitrate reduction (He et al., 2021), all calculations here were carried out at the DFT level using B3LYP exchange-correlation functional (Lee et al., 1988; Becke, 1993) with 6–31+g(d,p) basis set (Frisch et al., 1984). All structures were optimized to the local minimum with no imaginary frequency. Scaling factors were not considered since the systematic errors only influence the absolute β values but are mostly canceled out in the reported EIE and KIE values (Méheut et al., 2007; Schauble et al., 2006; Gao et al., 2018; He et al., 2020a; Li et al., 2021).

Anharmonic effect has been proposed to play a great role in vibrations involving light elements (Liu et al., 2010; Petts et al., 2015). However, in our previous calculations, we found that the anharmonic effect on the equilibrium nitrogen isotope fractionation between gaseous NH_4^+ and NH_3 was not significant (Li et al., 2021). Hayles et al. (2018) also found that the anharmonic corrections for the $^{18}\beta$ values of liquid and vapor water were small (2.53‰ and 2.96‰, respectively, at 25 °C), and the anharmonic correction for the *EIE* value between liquid water and water vapor was even smaller than 1‰. The anharmonic corrections for the *EIE* and *KIE* values of aqueous systems is expected to be partially canceled. In addition, to be comparable with the previous calculations (He et al., 2021), the anharmonic corrections were not applied in this study.

The new calculations performed in this study include the β factors for (1) isolated molecules without solvent effect, which is referred to as the gaseous (g) phase, (2) isolated molecules with implicit solvent effect by the integral-equation-formalism polarizable continuum model (IEFPCM), which is referred to as the IEFPCM model, and (3) molecules with the IEFPCM and explicit water molecules, which is referred to as aqueous (aq) phase or the hybrid-solvent models (see details below).

2.2. Solvent effects

The IEFPCM (Scalmani and Frisch, 2010) was included as the implicit solvent model, which can simulate the dielectric properties of solvent that affect the solute molecules. The explicit solvent molecules, which can cause large uncertainties on the local configuration and therefore the calculated β values, are simulated by the "water-droplet" model (Rustad et al., 2008, 2010; Zhang and Liu, 2014; Gao et al., 2018; Li et al., 2021). For all the water-droplet models, four starting clusters with 6 water molecules were built and optimized to local energy minimum as the first step. Subsequently, additional 6 water molecules were added to the outer shell of the optimized structures and optimized again to local energy minimum. This process was repeated until the calculated β value reached convergence, which occurred at 36 explicit water molecules in this study. This work used the hybrid-solvent model to include both short- and long-range solvent effects to simulate aqueous systems in a more realistic means (He et al., 2021; Li et al., 2021). The preferred values of β factors by the hybrid-solvent model are given as the average values of 12 models with 24–36 explicit water molecules.

2.3. Isotope fractionation theory

Based on the optimized structures, we calculated the β factors with the harmonic approximation for nitrogen and oxygen atoms of all species. The U–B-GM model (Urey, 1947; Bigeleisen and Goeppert Mayer, 1947) has been widely used for the calculations of β factors:

$$\beta = \prod_i^N \left(\frac{u_i^*}{u_i}\right)\left(\frac{e^{-u_i^*/2}}{e^{-u_i/2}}\right)\left(\frac{1-e^{-u_i}}{1-e^{-u_i^*}}\right) \quad (1)$$

$$u_i = \frac{h\upsilon_i}{k_B T} \quad (2)$$

where the superscript "*" indicates the rare isotope (^{15}N and ^{18}O) substituted molecules, the ones without superscript are the reference isotope (^{14}N and ^{16}O), ν_i denotes the *i*th harmonic vibration frequency, *h* denotes the Planck constant, k_B denotes the Boltzmann constant, *T* denotes the temperature in Kelvin, and *N* denotes the harmonic vibrational modes (for non-linear molecules, $N = 3n - 6$; for linear molecules, $N = 3n$-5; *n* is the total number of atoms). If a target species has more than one oxygen atom, the average values for all the oxygen atoms are reported since the observed isotope fractionations are compound-specific.

3. Results

Fig. 2 illustrates the optimized geometries for isolated NO_3^-, NO_2^-, and H_2O molecules with or without the IEFPCM (top panel), and the representative optimized geometries for $NO_3(H_2O)_{36}^-$, $NO_2(H_2O)_{36}^-$, and $H_2O(H_2O)_{36}$ configurations (bottom panel). The selected geometry parameters for aqueous phases are the average values of the 12 models with 24–36 explicit water molecules. Detailed geometry parameters are listed in Table S1 – S2 of SI. Among the three oxygen atoms in NO_3^-, O_a, O_b, and O_c denote O2, O3, and O4 atoms in structure coordinates, respectively. Among the two oxygen atoms in NO_2^-, O_a and O_b denote O2 and O3 atoms in structure coordinates, respectively (See SI for the optimized structure coordinates).

3.1. NO_3^- in aqueous phase

For NO_3^-, the calculations yielded 1.26(5) Å for the N–O bond length ($d_{N-O(NO_3^-)}$) and 120.0° for the $\angle ONO_{NO_3^-}$ angle in gaseous phase, 1.26(3) Å for $d_{N-O(NO_3^-)}$ and 120.0° ± 0.6° for $\angle ONO_{NO_3^-}$ in the IEFPCM model, and an average value of 1.26(0) ± 0.01 Å for $d_{N-O(NO_3^-)}$ and an average value of 120.0° ± 0.6° for $\angle ONO_{NO_3^-}$ in aqueous phase (Fig. 2). These results are consistent with previous theoretical calculation and experimental results, e.g., $d_{N-O(NO_3^-)}$ = 1.23–1.29 Å and $\angle ONO_{NO_3^-}$ = 120° in solutions (Megyes et al., 2009; Vchirawongkwin et al., 2011; Wang et al., 2018).

Table 1 lists the calculated β values of NO_3^- at 25 °C using the three models. The modeling for gaseous phase yielded ${}^{15}\beta_{NO_{3(g)}^-}$ = 1.1558 and ${}^{18}\beta_{NO_{3(g)}^-}$ = 1.0931. The IEFPCM causes a 4.6‰ decrease in the ${}^{15}\beta_{NO_3^-}$ value with ${}^{15}\beta_{NO_{3(IEFPCM)}^-}$ = 1.1505, but only 0.2‰ decrease in the ${}^{18}\beta_{NO_3^-}$ value with ${}^{18}\beta_{NO_{3(IEFPCM)}^-}$ = 1.0929. The preferred β values of NO_3^- in aqueous phase are ${}^{15}\beta_{NO_{3(aq)}^-}$ = 1.1577 and ${}^{18}\beta_{NO_{3(aq)}^-}$ = 1.0995. Compared to the results of gaseous phase, the hybrid-solvent effect causes a small increase of 1.6‰ in the ${}^{15}\beta_{NO_3^-}$ value, but a larger increase of 5.9‰ in the ${}^{18}\beta_{NO_{3(aq)}^-}$ value.

3.2. NO_2^- in aqueous phase

For NO_2^-, the calculations yielded $d_{N-O(NO_2^-)}$ = 1.26(4) Å and $\angle ONO_{NO_2^-}$ = 116.5° in gaseous phase, $d_{N-O(NO_2^-)}$ = 1.26(2) Å and $\angle ONO_{NO_3^-}$ = 116.1° in the IEFPCM model, and an average $d_{N-O(NO_2^-)}$ = 1.26(1) ± 0.01 Å and an average $\angle ONO_{NO_2^-}$ = 115.4° ± 0.4° in aqueous phase (Fig. 2). These results are consistent with previous theoretical calculation and experimental results, e.g., $d_{N-O(NO_2^-)}$ = 1.24–1.26 Å and $\angle ONO_{NO_2^-}$ = 115° – 116° (Boxe et al., 2006; Wei et al., 2013).

Table 2 lists the calculated β values of NO_2^- at 25 °C for the three models. The models in gaseous phase gave ${}^{15}\beta_{NO_{2(q)}^-}$ = 1.0938 and ${}^{18}\beta_{NO_{2(g)}^-}$ = 1.0803. The IEFPCM causes a 2.0‰ decrease in the ${}^{15}\beta_{NO_2^-}$ value with ${}^{15}\beta_{NO_{2(IEFPCM)}^-}$ = 1.0917, and a 0.3‰ decrease in the ${}^{18}\beta_{NO_2^-}$ value with ${}^{18}\beta_{NO_{2(IEFPCM)}^-}$ = 1.0799. The preferred β values of NO_2^- in aqueous phase are ${}^{15}\beta_{NO_{2(aq)}^-}$ = 1.1009 and ${}^{18}\beta_{NO_{2(aq)}^-}$ = 1.0892. Compared to the results of gaseous phase, the hybrid-solvent effects have greater influence on both ${}^{15}\beta_{NO_2^-}$ values (6.5‰) and ${}^{18}\beta_{NO_2^-}$ value (8.2‰) than those of NO_3^-.

3.3. H_2O in aqueous phase

For H_2O molecule, the calculations yielded $d_{O\text{-}H}$ = 0.96(4) Å and $\angle HOH$ = 105.7° in gaseous phase, $d_{O\text{-}H}$ = 0.96(7) Å and $\angle HOH$ = 105.0° in the IEFPCM model, and an average $d_{O\text{-}H}$ = 0.98(3) ± 0.01 Å and an average $\angle HOH$ = 106.3° ± 1.7° in aqueous phase (Fig. 2 and Table 3). These calculation results are consistent with previous laboratory experiments and theoretical calculations, which gave $d_{O\text{-}H}$ = 0.957–0.977 Å and $\angle HOH$ = 103.8° – 107.7° in gaseous phase (Walford et al., 1977; Xantheas, 1995; Alhambra et al., 1998; Császár et al., 2005; Fanourgakis and Xantheas, 2006a; Méheut et al., 2007), and $d_{O\text{-}H}$ = 0.955–0.985 Å

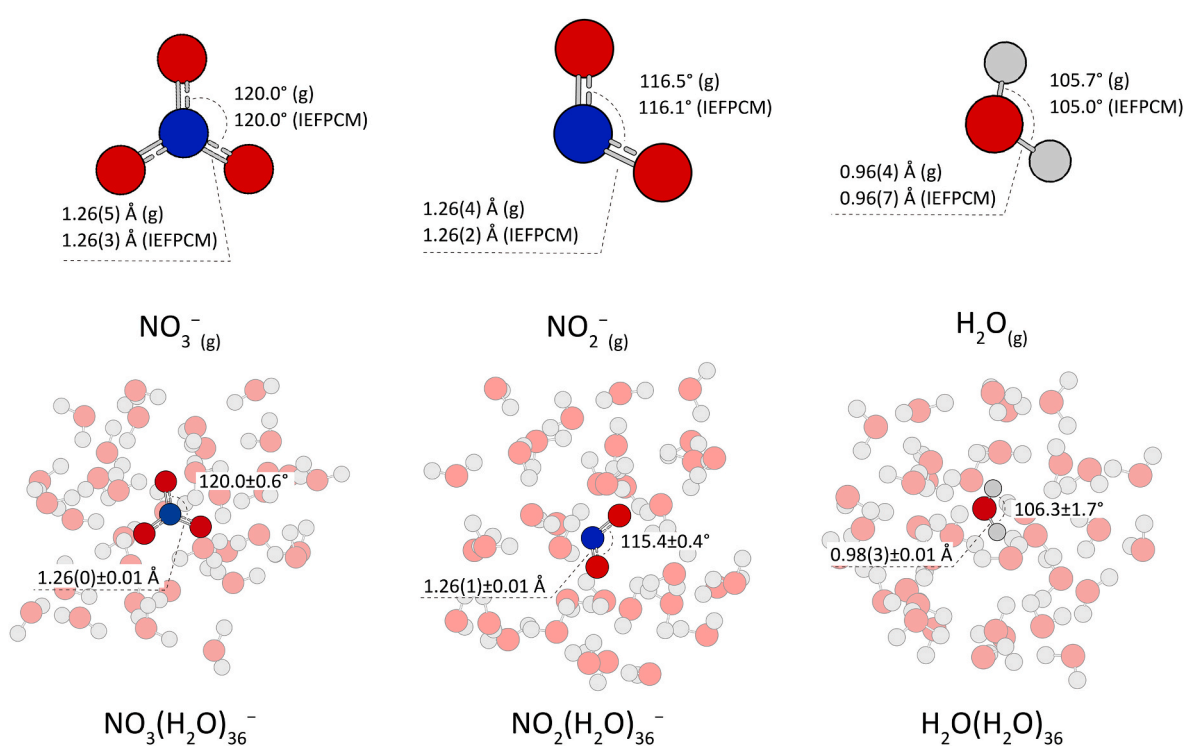

Fig. 2. Representative configurations of NO_3^-, NO_2^-, H_2O, $NO_3(H_2O)_{36}^-$, $NO_2(H_2O)_{36}^-$, and $H_2O(H_2O)_{36}$. The color code is the same as in Fig. 1. The bond lengths and angles for aqueous phases are the averages of 12 models with 24–36 water molecules.

Table 1
The calculated $\beta_{NO_3^-}$ factors of nitrate at 25 °C in gaseous phase, by the IEFPCM model, and by the hybrid-solvent model.

Model	$^{15}\beta$	$^{18}\beta_a$	$^{18}\beta_b$	$^{18}\beta_c$	$^{18}\beta_{ave}$[a]
$NO_3^-{}_{(g)}$	**1.1558**	1.0931	1.0931	1.0931	**1.0931**
lnβ (‰)	**144.8**				**89.0**
$NO_3^-{}_{(IEFPCM)}$	**1.1505**	1.0929	1.0929	1.0929	**1.0929**
lnβ (‰)	**140.2**				**88.8**
$NO_3(H_2O)_6^-$_A	1.1551	1.0983	1.0983	1.0984	1.0983
$NO_3(H_2O)_6^-$_B	1.1553	1.1006	1.0957	1.0975	1.0979
$NO_3(H_2O)_6^-$_C	1.1543	1.0952	1.0972	1.0973	1.0966
$NO_3(H_2O)_6^-$_D	1.1551	1.0976	1.0991	1.0983	1.0983
Average[b]	1.1550 ± 0.0004				1.0978 ± 0.0014
$NO_3(H_2O)_{12}^-$_A	1.1552	1.0957	1.0966	1.0998	1.0974
$NO_3(H_2O)_{12}^-$_B	1.1552	1.0974	1.0970	1.0985	1.0976
$NO_3(H_2O)_{12}^-$_C	1.1559	1.0996	1.0964	1.0955	1.0972
$NO_3(H_2O)_{12}^-$_D	1.1556	1.0979	1.0976	1.0968	1.0974
Average	1.1555 ± 0.0003				1.0974 ± 0.0014
$NO_3(H_2O)_{18}^-$_A	1.1572	1.0975	1.0972	1.1015	1.0987
$NO_3(H_2O)_{18}^-$_B	1.1562	1.0971	1.0959	1.1008	1.0979
$NO_3(H_2O)_{18}^-$_C	1.1560	1.0987	1.0985	1.0945	1.0972
$NO_3(H_2O)_{18}^-$_D	1.1563	1.0954	1.0993	1.1002	1.0983
Average	1.1564 ± 0.0005				1.0981 ± 0.0022
$NO_3(H_2O)_{24}^-$_A	1.1586	1.0989	1.0998	1.1023	1.1003
$NO_3(H_2O)_{24}^-$_B	1.1568	1.0973	1.0968	1.0997	1.0979
$NO_3(H_2O)_{24}^-$_C	1.1571	1.1005	1.0975	1.0967	1.0982
$NO_3(H_2O)_{24}^-$_D	1.1571	1.0997	1.0956	1.1033	1.0995
Average	1.1574 ± 0.0008				1.0990 ± 0.0023
$NO_3(H_2O)_{30}^-$_A	1.1581	1.0980	1.1000	1.1006	1.0995
$NO_3(H_2O)_{30}^-$_B	1.1579	1.0982	1.1024	1.0993	1.1000
$NO_3(H_2O)_{30}^-$_C	1.1578	1.1028	1.0963	1.0993	1.0995
$NO_3(H_2O)_{30}^-$_D	1.1575	1.1013	1.0967	1.1015	1.0998
Average	1.1578 ± 0.0002				1.0997 ± 0.0021
$NO_3(H_2O)_{36}^-$_A	1.1583	1.0976	1.0986	1.1026	1.0996
$NO_3(H_2O)_{36}^-$_B	1.1580	1.0993	1.0980	1.1020	1.0998
$NO_3(H_2O)_{36}^-$_C	1.1574	1.1019	1.0962	1.1004	1.0995
$NO_3(H_2O)_{36}^-$_D	1.1577	1.1017	1.0966	1.1014	1.0999
Average	1.1579 ± 0.0004				1.0997 ± 0.0023
Preferred value[c]	**1.1577**				**1.0995**
lnβ (‰)	**146.4**				**94.9**

[a] The $^{18}\beta_{ave}$ values are the mean values of $^{18}\beta_a$, $^{18}\beta_b$, and $^{18}\beta_c$.
[b] The "Average" data are the mean values of the four models with the same numbers of explicit water molecules, same below.
[c] The "preferred value" for aqueous phase is the average result of 12 models with 24–36 explicit water molecules, same below.

and ∠HOH = 104.0° – 107.5° in aqueous phase (Walford et al., 1977; Narten and Levy, 1971; Powles, 1981; Ichikawa et al., 1991; Xantheas, 1995; Alhambra et al., 1998; Silvestrelli and Parrinello, 1999; Császár et al., 2005; Fanourgakis and Xantheas, 2006a, b; Méheut et al., 2007). Our new results also verify previous observations that, compared with those of a monomer H_2O molecule, the $d_{O\text{-}H}$ and ∠HOH increase in liquid water (Walford et al., 1977; Xantheas, 1995; Fanourgakis and Xantheas, 2006a, b).

Table 4 lists the calculated $^{18}\beta$ values of H_2O at 25 °C for the three models. A $^{18}\beta_{H_2O_{(g)}}$ value of 1.0658 was yielded for gaseous phase model. The IEFPCM caused a decrease of 0.4‰ with $^{18}\beta_{H_2O_{(IEFPCM)}} = 1.0658$. The hybrid-solvent effects caused a difference of 10.2‰ between $^{18}\beta_{H_2O_{(g)}}$ and $^{18}\beta_{H_2O_{(aq)}}$, where the preferred $^{18}\beta_{H_2O_{(aq)}}$ value is 1.0771.

3.4. Temperature-dependent equilibrium isotope fractionation factors

The general equations describing the temperature-dependent β values for individual species are given in Table 5 and plotted in Fig. 3.

Table 2
The calculated $\beta_{NO_2^-}$ factors of nitrite in gaseous phase, by the IEFPCM model, and by the hybrid-solvent model at 25 °C.

Model	$^{15}\beta$	$^{18}\beta_a$	$^{18}\beta_b$	$^{18}\beta_{ave}$[a]
$NO_2^-{}_{(g)}$	**1.0938**	1.0803	1.0803	**1.0803**
lnβ (‰)	**89.7**			**77.2**
$NO_2^-{}_{(IEFPCM)}$	**1.0917**	1.0799	1.0799	**1.0799**
lnβ (‰)	**87.7**			**76.9**
$NO_2(H_2O)_6^-$_A	1.1001	1.0888	1.0864	1.0876
$NO_2(H_2O)_6^-$_B	1.1029	1.0896	1.0881	1.0889
$NO_2(H_2O)_6^-$_C	1.0994	1.0903	1.0861	1.0882
$NO_2(H_2O)_6^-$_D	1.1004	1.0900	1.0877	1.0889
Average	1.1007 ± 0.0015			1.0884 ± 0.0016
$NO_2(H_2O)_{12}^-$_A	1.1022	1.0906	1.0884	1.0895
$NO_2(H_2O)_{12}^-$_B	1.1016	1.0838	1.0901	1.0870
$NO_2(H_2O)_{12}^-$_C	1.0986	1.0842	1.0857	1.0850
$NO_2(H_2O)_{12}^-$_D	1.0959	1.0871	1.0837	1.0854
Average	1.0996 ± 0.0029			1.0867 ± 0.0028
$NO_2(H_2O)_{18}^-$_A	1.1003	1.0916	1.1003	1.0960
$NO_2(H_2O)_{18}^-$_B	1.1028	1.0908	1.0886	1.0897
$NO_2(H_2O)_{18}^-$_C	1.0966	1.0875	1.0862	1.0869
$NO_2(H_2O)_{18}^-$_D	1.1026	1.0879	1.0897	1.0888
Average	1.1006 ± 0.0029			1.0903 ± 0.0044
$NO_2(H_2O)_{24}^-$_A	1.1027	1.0937	1.0850	1.0894
$NO_2(H_2O)_{24}^-$_B	1.1019	1.0887	1.0911	1.0899
$NO_2(H_2O)_{24}^-$_C	1.0973	1.0886	1.0873	1.0880
$NO_2(H_2O)_{24}^-$_D	1.1014	1.0894	1.0889	1.0892
Average	1.1008 ± 0.0024			1.0891 ± 0.0026
$NO_2(H_2O)_{30}^-$_A	1.1015	1.0887	1.0880	1.0884
$NO_2(H_2O)_{30}^-$_B	1.1022	1.0909	1.0887	1.0898
$NO_2(H_2O)_{30}^-$_C	1.0991	1.0882	1.0928	1.0905
$NO_2(H_2O)_{30}^-$_D	1.1012	1.0889	1.0885	1.0887
Average	1.1010 ± 0.0013			1.0893 ± 0.0017
$NO_2(H_2O)_{36}^-$_A	1.1016	1.0888	1.0882	1.0885
$NO_2(H_2O)_{36}^-$_B	1.1028	1.0891	1.0894	1.0893
$NO_2(H_2O)_{36}^-$_C	1.0987	1.0879	1.0914	1.0897
$NO_2(H_2O)_{36}^-$_D	1.1017	1.0896	1.0886	1.0891
Average	1.1012 ± 0.0018			1.0891 ± 0.0011
Preferred value	**1.1010**			**1.0892**
lnβ (‰)	**96.2**			**85.4**

[a] The $^{18}\beta_{ave}$ values are the mean values of $^{18}\beta_a$ and $^{18}\beta_b$.

The β values in both gaseous and aqueous phases share the same pattern. For all three molecules, the hybrid-solvent effects induced increases in the β values of both ^{15}N and ^{18}O, with a greater influence on ^{18}O than ^{15}N. The values $^{15}\beta_{NO_3^-}$ are greater than the $^{15}\beta_{NO_2^-}$ values at 0–300 °C. The $^{18}\beta$ values follow the order of $NO_3^- > NO_2^- > H_2O$ below ~200 °C, but change to $NO_3^- > H_2O > NO_2^-$ when the temperature is greater than ~200 °C.

The general equations describing the temperature-dependent ln*EIE* values of ^{15}N and ^{18}O for the NO_3^-–NO_2^- pair and the H_2O–NO_2^- pair in gaseous and aqueous phases are given in Table 6. The calculations for gaseous phase, the IEFPCM model and the hybrid-solvent model yielded fractionation factors at 25 °C as the values are +55.1‰, +52.5‰, and +50.2‰ for $\ln^{15}EIE_{(NO_3^- - NO_2^-)}$, +11.8‰, +12.0‰, and +9.4‰ for $\ln^{18}EIE_{(NO_3^- - NO_2^-)}$, and −13.1‰, −13.1‰, and −11.2‰ for $\ln^{18}EIE_{(H_2O - NO_2^-)}$, respectively.

4. Discussions and implications

4.1. Oxygen isotope equilibrium fractionation between liquid and vapor water

The calculated $^{18}\beta_{H_2O(g)}$ value of 1.0658 at 25 °C agrees well with previously reported values of 1.064–1.068 (Urey, 1947; Saxena et al., 1962; Thornton, 1962; Bottinga, 1968; Richet et al., 1977; Walters and Michalski, 2016; Hayles et al., 2018; Zeebe, 2020). In comparison, Hayles et al. (2018) calculated the $^{18}\beta_{H_2O(aq)}$ value using water clusters with 22 H_2O molecules without implicit solvent effect. Their results

Table 3
Comparison of geometry parameters (d – distances in Å, ∠– angles in °) for H_2O in gaseous and aqueous phases from this work and previous studies.

$d_{O\text{-}H}$ (Å)		∠HOH (°)		Methods and References
Gaseous	Aqueous	gaseous	aqueous	
0.96(4)	**0.98(3) ± 0.01**	**105.7**	**106.3 ± 1.7**	**DFT, this work**
0.958	0.98 ± 0.01	104.5	105.5 ± 3.3	Neutron diffraction (Walford et al., 1977)
0.965	0.972–0.985	103.8	104.2–105.3	DFT (Xantheas, 1995)
0.966–0.973	0.955–0.975	105.5–107.7	104.2–107.5	molecular orbital-Monte Carlo and molecular dynamics (Alhambra et al., 1998)
0.957	0.968	104.52	106.3 ± 4.9	Molecular Dynamics (Fanourgakis and Xantheas, 2006a, b)
0.958		104.5		DFT (Császár et al., 2005)
0.974–0.977		104.1–105.0		DFT (Méheut et al., 2007)
	0.9763		106	X-Ray Diffraction (Narten and Levy, 1971)
	0.983 ± 0.008		104 ± 2	Slow neutron scattering (Powles, 1981)
	0.970 ± 0.005		106.1 ± 1.8	Neutron-diffraction (Ichikawa et al., 1991)
	0.972		104.4	Molecular Dynamics (Silvestrelli and Parrinello, 1999)

Table 4
The calculated $^{18}\beta_{H_2O}$ factors of water in gaseous phase, by the IEFPCM model and the hybrid-solvent model at 25 °C.

Model	$^{18}\beta$	Model	$^{18}\beta$
$H_2O_{(g)}$	**1.0662**	**lnβ (‰)**	**64.1**
$H_2O_{(IEFPCM)}$	**1.0658**	**lnβ (‰)**	**63.7**
$H_2O(H_2O)_6$_A	1.0791	$H_2O(H_2O)_{24}$_A	1.0771
$H_2O(H_2O)_6$_B	1.0798	$H_2O(H_2O)_{24}$_B	1.0792
$H_2O(H_2O)_6$_C	1.0761	$H_2O(H_2O)_{24}$_C	1.0782
$H_2O(H_2O)_6$_D	1.0756	$H_2O(H_2O)_{24}$_D	1.0782
Average[1]	1.0777 ± 0.0021	Average	1.0782 ± 0.0009
$H_2O(H_2O)_{12}$_A	1.0756	$H_2O(H_2O)_{30}$_A	1.0792
$H_2O(H_2O)_{12}$_B	1.0752	$H_2O(H_2O)_{30}$_B	1.0767
$H_2O(H_2O)_{12}$_C	1.0771	$H_2O(H_2O)_{30}$_C	1.0768
$H_2O(H_2O)_{12}$_D	1.0791	$H_2O(H_2O)_{30}$_D	1.0752
Average	1.0768 ± 0.0018	Average	1.0770 ± 0.0017
$H_2O(H_2O)_{18}$_A	1.0753	$H_2O(H_2O)_{36}$_A	1.0763
$H_2O(H_2O)_{18}$_B	1.0801	$H_2O(H_2O)_{36}$_B	1.0765
$H_2O(H_2O)_{18}$_C	1.0778	$H_2O(H_2O)_{36}$_C	1.0753
$H_2O(H_2O)_{18}$_D	1.0794	$H_2O(H_2O)_{36}$_D	1.0760
Average	1.0782 ± 0.0021	Average	1.0760 ± 0.0005
Preferred value	**1.0771**		
lnβ (‰)	**74.3**		

showed that, at 25°C, using the B3LYP/6-311+G(d) level of theory, the calculated $^{18}\beta_{H_2O}$ values increased from 1.0660 in gaseous phase to 1.0764 in aqueous phase; using the B3LYP/6-311+G*(2df,p) level of theory, the calculated $^{18}\beta_{H_2O}$ values increased from 1.0659 in gaseous phase to 1.0733 in aqueous phase (Hayles et al., 2018). Zeebe (2020) also calculated the $^{18}\beta_{H_2O(aq)}$ value using water clusters with 4–17 H_2O molecules without implicit solvent effect. His results showed that, at 25 °C, using the X3LYP/6-311+G(d,p) level of theory, the calculated $^{18}\beta_{H_2O}$ values increased from 1.0662 for an isolated water molecule in gaseous phase to 1.0753 for the $H_2O(H_2O)_4$ model to 1.0766 for the $H_2O(H_2O)_{17}$ model; using the MP2/aug-cc-pVDZ level of theory, the calculated $^{18}\beta_{H_2O}$ values increased from 1.0659 for an isolated water molecule to 1.0738 for the $H_2O(H_2O)_4$ model to 1.0752 for the $H_2O(H_2O)_8$ model (Zeebe, 2020). Our results are comparable with those of Hayles et al. (2018) and Zeebe (2020) who used higher theoretical levels, which indicates that our choice of calculation method is sufficient. The calculations in above two studies did not consider the configurational disorder of liquid water. Our results showed that the four configurations with the same numbers of explicit water molecules have standard deviations of ±0.0005 to ±0.0021 (Table 4), indicating that the interactions between water molecules have a significant influence on local configurations. Therefore, we prefer to use the average values of the 12 configurations with 24–36 explicit water molecules ($^{18}\beta_{H_2O(aq)}$ = 1.0771), which can minimize the local uncertainty associated with individual configurations.

Table 5
Polynomial fit parameters of calculated lnβ values of ^{15}N and ^{18}O for NO_3^-, NO_2^-, and H_2O in the gaseous phase, by the IEFPCM model, and in the aqueous phase at 0–300 °C as the form of $1000\ln\beta = a + bx + cx^2 + dx^3$, in which $x = 10^6/T^2$ and T is the temperature in Kelvin.

Element	Species	a	b	c	d
$1000\ln^{15}\beta$	$NO_3^-{}_{(g)}$	2.8988	17.3010	−0.5449	0.0114
	$NO_3^-{}_{(IEFPCM)}$	2.5564	16.68	−0.5164	0.0108
	$NO_3^-{}_{(aq)}$	2.9314	17.5240	−0.5561	0.0117
	$NO_2^-{}_{(g)}$	1.7880	10.7800	−0.3438	0.0071
	$NO_2^-{}_{(IEFPCM)}$	1.5400	10.5760	−0.3397	0.0072
	$NO_2^-{}_{(aq)}$	1.9007	11.5390	−0.3676	0.0077
$1000\ln^{18}\beta$	$NO_3^-{}_{(g)}$	0.6534	10.2000	−0.2680	0.0053
	$NO_3^-{}_{(IEFPCM)}$	0.7986	10.0940	−0.2569	0.0049
	$NO_3^-{}_{(aq)}$	0.9820	10.7190	−0.2694	0.0052
	$NO_2^-{}_{(g)}$	1.3680	8.9752	−0.2527	0.0048
	$NO_2^-{}_{(IEFPCM)}$	1.0431	9.0197	−0.2618	0.0052
	$NO_2^-{}_{(g)}$	1.2524	9.8842	−0.2763	0.0056
	$H_2O_{(g)}$	7.9504	7.7902	−0.3474	0.0087
	$H_2O_{(IEFPCM)}$	8.1079	7.6692	−0.3372	0.0084
	$H_2O_{(aq)}$	7.0634	8.6720	−0.3326	0.0082

The calculated $^{18}EIE_{H_2O_{(aq)}-H_2O_{(g)}}$ value of 1.0102 at 25 °C is also consistent with previously published data, with a difference smaller than 1‰ to the calculation results of 1.0068–1.0098 by Hayles et al. (2018) and 1.0084–1.0098 by Zeebe (2020), and the experimental results of 1.0094 by Majoube (1971), 1.0097 by Horita and Wesolowski (1994), and 1.0094 by Barkan and Luz (2005). Uncertainties of this magnitude can be considered small and adequate for the current purpose.

4.2. Equilibrium isotope fractionations between NO_3^- and NO_2^-

The calculated β factors and ln $EIE_{NO_3^--NO_2^-}$ values at 25 °C from this study and literature are compiled in Table 7. For both NO_3^- and NO_2^- in gaseous phases, our calculated $^{15}\beta$ factors are higher than those of Begun and Fletcher (1960), Stern et al. (1962), and Monse et al. (1969), but lower than those of Spindel (1954) and Walters and Michalski (2015). The $\ln^{15}EIE_{NO_3^--NO_2^-}$ values of gaseous phases at 25 °C obtained in this study is +55.1‰, which is lower than previous calculation results in the range of +57.4‰ ~ +86.6‰ (Fig. 4; Table 7). Compared to the models in gaseous phases, the IEFPCM models yielded a slight decrease in the $\ln^{15}EIE_{NO_3^--NO_2^-}$ value, e.g., from +60.0‰ to +56.1‰ in Casciotti (2009), from +57.4‰ to +54.0‰ in Walters and Michalski (2015), and from +55.1‰ to +52.5‰ in this study. Compared to NO_3^-, the $^{15}\beta$ factors of

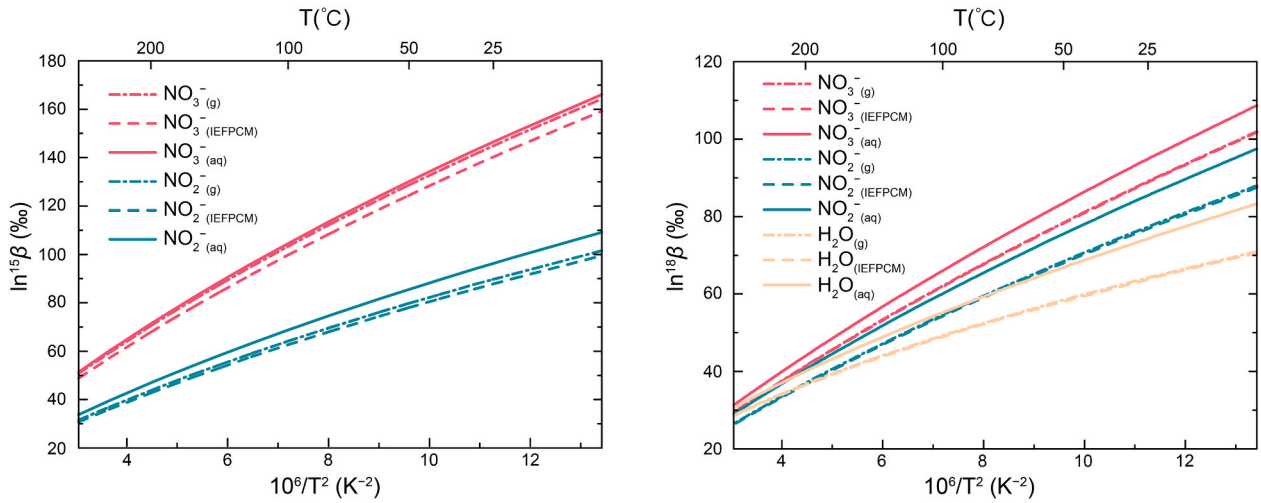

Fig. 3. Temperature dependence of lnβ values in per mil (‰) of ^{15}N (left) and ^{18}O (right) for NO_3^-, NO_2^-, and H_2O in aqueous phase in 0–300 °C.

Table 6
Polynomial fit parameters of calculated 1000ln*EIE* values of ^{15}N and ^{18}O among NO_3^-, H_2O, and NO_2^- in gaseous and aqueous phases at 0–300 °C as the form of $1000\ln EIE = a + bx + cx^2 + dx^3$, in which $x = 10^6/T^2$ and T is the temperature in Kelvin.

Element	Species	*a*	*b*	*c*	*d*	ln*EIE* (‰, 25 °C)
1000ln^{15}*EIE*	$NO_3^-{}_{(g)} - NO_2^-{}_{(g)}$	1.1109	6.5215	−0.2011	0.0043	+55.1
	$NO_3^-{}_{(IEFPCM)} - NO_2^-{}_{(IEFPCM)}$	1.0163	6.1044	−0.1767	0.0036	+52.5
	$NO_3^-{}_{(aq)} - NO_2^-{}_{(aq)}$	1.0307	5.9852	−0.1884	0.004	+50.2
1000ln^{18}*EIE*	$NO_3^-{}_{(g)} - NO_2^-{}_{(g)}$	−0.7146	1.2246	−0.0153	0.0004	+11.8
	$NO_3^-{}_{(IEFPCM)} - NO_2^-{}_{(IEFPCM)}$	−0.2445	1.0739	0.0049	−0.0003	+12.0
	$NO_3^-{}_{(aq)} - NO_2^-{}_{(aq)}$	−0.2705	0.8345	0.0068	−0.0004	+9.4
	$H_2O_{(g)} - NO_2^-{}_{(g)}$	6.5824	−1.185	−0.0946	0.0039	−13.1
	$H_2O_{(IEFPCM)} - NO_2^-{}_{(IEFPCM)}$	7.0648	−1.3505	−0.0754	0.0032	−13.1
	$H_2O_{(aq)} - NO_2^-{}_{(aq)}$	5.8109	−1.2122	−0.0564	0.0026	−11.2

Table 7
Comparison of calculated β factors of nitrate and nitrite and $\ln EIE_{NO_3^- - NO_2^-}$ (‰) at 25 °C between this study and previous theoretical calculations and laboratory experiments.

Model	$^{15}\beta_{NO_3^-}$	$^{15}\beta_{NO_2^-}$	$\ln^{15}EIE_{NO_3^- - NO_2^-}$ (‰)	$^{18}\beta_{NO_3^-}$	$^{18}\beta_{NO_2^-}$	$\ln^{15}EIE_{NO_3^- - NO_2^-}$ (‰)	Source
Gaseous	**1.1558**	**1.0938**	**+55.1**	**1.0931**	**1.0803**	**+11.8**	**This work**
	1.169	1.072	+86.6				Spindel (1954)
	1.1506	1.0803	+63.0				Begun and Fletcher (1960)
	1.15	1.08	+62.8				Stern et al. (1962)
	1.1505	1.0847	+58.9	1.0938	1.0818	+11.0	Monse et al. (1969)
			+60.0				Casciotti (2009)
	1.1588	1.0942	+57.4	1.0904	1.0918	−1.3	(Walters and Michalski, 2015, 2016)[a]
IEFPCM	**1.1505**	**1.0917**	**+52.5**	**1.0929**	**1.0799**	**+12.0**	**This work**
			+56.1				(Casciotti, 2009)[b]
	1.1525	1.0919	+54.0				Walters and Michalski (2015)
Aqueous	**1.1577**	**1.1009**	**+50.3**	**1.0995**	**1.0892**	**+9.4**	**This work**

[a] Calculations in Walters and Michalski (2015) were based on the B3LYP/cc-pVTZ and EDF2/cc-pVTZ levels of theory. Calculations in Walters and Michalski (2016) were based on the B3LYP/cc-pVTZ, EDF2/cc-pVTZ, QCISD/cc-pVDZ, and EOM-CCSD/aug-cc-pVDZ levels of theory. All the calculation results have similar β-T correlations. Here we only use the B3LYP/cc-pVTZ results calculated based on the polynomial fits.

[b] The calculations in Casciotti (2009) were based on the B3LYP/6-31g(d) level of theory in gaseous phase and "*aqueous solution*". The calculation details of the aqueous phase were not given in the study, but the results are reproducible by the IEFPCM solvent model without explicit solvent molecules.

NO_2^- is more affected by the explicit solvent effect, which consequently produced a much smaller $\ln^{15}EIE_{NO_3^- - NO_2^-}$ value (+50.3‰) by the hybrid-solvent model. These results are smaller than the experimental results of anaerobic ammonium oxidation (anammox, +62.4‰ ± 1.0‰, Brunner et al., 2013).

Available data for the $^{18}\beta$ factors of NO_3^- and NO_2^- are relatively few (Table 7). Our calculated $^{18}\beta$ factors and $\ln^{18}EIE_{NO_3^- - NO_2^-}$ values in gaseous phase (e.g., +11.8‰ at 25 °C) are consistent with the results of Monse et al. (1969) (Table 7 and Fig. 5). In contrast, Walters and Michalski (2016) reported a negative $\ln^{18}EIE_{NO_3^- - NO_2^-}$ value of −1.3‰ at 25 °C. This difference is mainly caused by the significantly higher $^{18}\beta_{NO_2^-}$ value (1.0918 at 25 °C) and slightly lower $^{18}\beta_{NO_3^-}$ value (1.0904 at 25 °C) in Walters and Michalski (2016) than those in Monse et al. (1969) and this study. Laboratory experiments gave $\ln^{18}EIE_{NO_3^- - H_2O}$ of +21.3‰ (Böhlke et al., 2003) and $\ln^{18}EIE_{H_2O - NO_2^-}$ of −13.4‰ to −13.7‰ (Casciotti et al., 2007; Buchwald and Casciotti, 2013) at 22 °C, from which

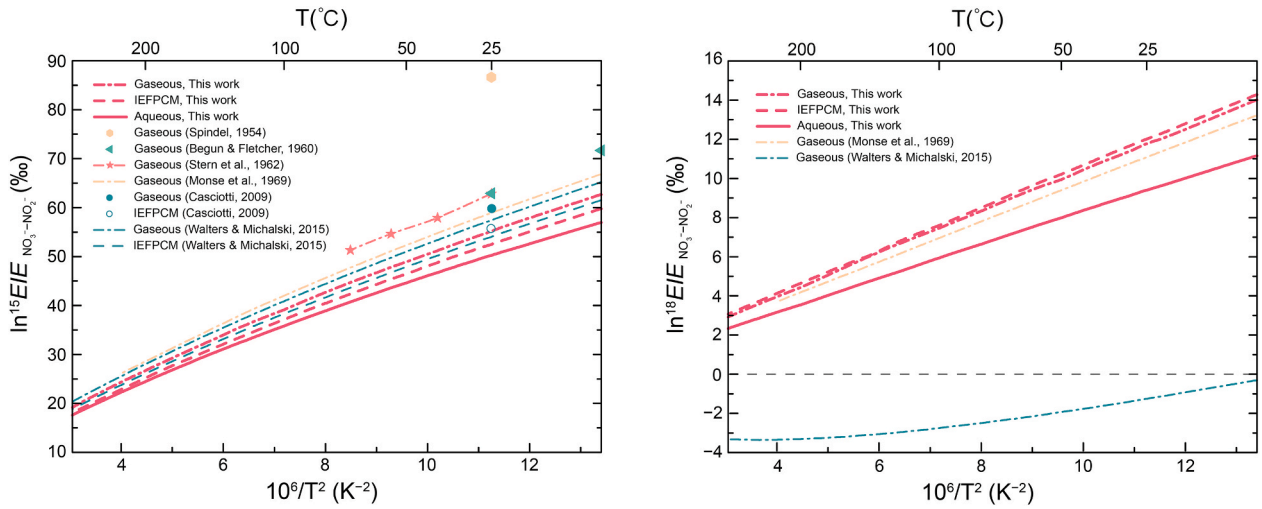

Fig. 4. Comparison of temperature-dependent $\ln^{15}EIE_{NO_3^- - NO_2^-}$ (left) and $\ln^{18}EIE_{NO_3^- - NO_2^-}$ (right) values at 0–300 °C between this study and previous results from theoretical calculations and laboratory experiments.

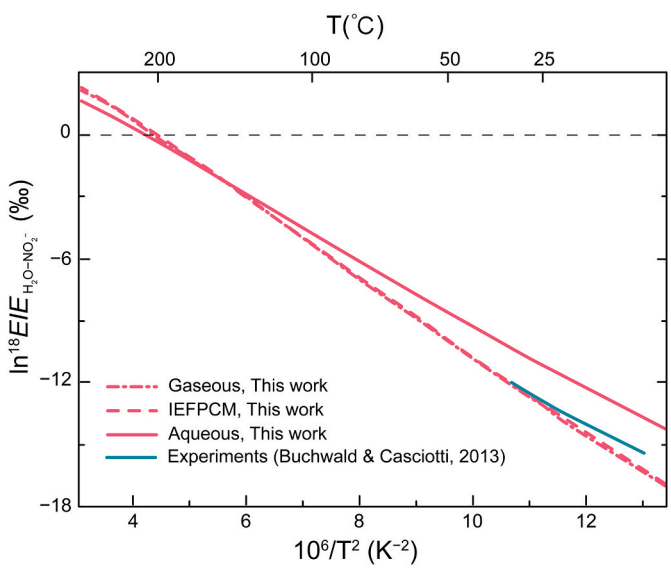

Fig. 5. Temperature-dependent $\ln^{18}EIE_{H_2O-NO_2^-}$ values at 0–300 °C.

the $\ln^{18}EIE_{NO_3^- - NO_2^-}$ value can be derived to be +7.6‰ to +7.9‰ at 22 °C. Our calculations obtained $\ln^{18}EIE_{NO_3^- - H_2O(aq)} = +21.1‰$ and $\ln^{18}EIE_{H_2O-NO_2^-(aq)} = -11.5‰$ at 22 °C, which are consistent with the experimental results. Walters and Michalski (2016) also reported $\ln^{18}EIE_{NO_3^- - H_2O} = +25.2‰$at 22 °C with $^{18}\beta_{H_2O} = 1.0647$, which is close to the experimental results. However, their calculated $\ln^{18}EIE_{H_2O-NO_2^-} = -26.4‰$ and $\ln^{18}EIE_{NO_3^- - NO_2^-} = -1.2‰$at 22 °C are very different from the experimental results. The reason for this significant discrepancy is difficult to assess at the moment due to the lack of optimized structures and vibrational frequencies in Walters and Michalski (2016). Therefore, in the following discussion, we do not include the results of Walters and Michalski (2016).

4.3. Oxygen isotope equilibrium fractionation between H_2O and NO_2^-

Nitrite is an essential intermediate in marine nitrogen cycle and can accumulate locally to a pronounced level (Dore and Karl, 1996; Lipschultz et al., 1996). Since the oxygen atom exchange between nitrite and ambient water is in the order of weeks to months, the isotope composition of nitrite can be used to estimate the rate of biochemical processes that occur on these time scales (Buchwald and Casciotti, 2013). If nitrite is in equilibrium with water, oxidation of nitrite would introduce more water oxygen into nitrate, which would influence the $\delta^{18}O_{NO_3^-}$ value and consequently the observed isotope fractionation factors of nitrate reduction. Therefore, the $\ln^{18}EIE_{H_2O-NO_2^-}$ value is an important parameter for modeling the biological nitrogen cycle, particularly in quantifying the rates and contribution of nitrite oxidation, as well as providing constraints on the isotope effect during nitrate reduction.

Previous experiments showed that the equilibrium isotope fractionation factors between nitrite and water at 277–306 K can be described as (Buchwald and Casciotti, 2013, equation (2)):

$$^{18}\varepsilon_{eq} \times 1000 = \left(^{18}O/^{16}O\right)_{NO_2,eq} \div \left(^{18}O/^{16}O\right)_{H_2O,eq} - 1 = -0.12T + 48.79$$

from which the $\ln^{18}EIE_{H_2O-NO_2^-}$ value can be derived to be −12.9‰ at 25 °C. This value (Fig. 5, green line) lies between our calculated $\ln^{18}EIE_{H_2O-NO_2^-}$ values for gaseous (−13.1‰ at 25 °C) and aqueous phases (−11.2‰ at 25 °C). The overall distribution of the experimental results (Buchwald and Casciotti, 2013) parallel to the calculation results of aqueous phase, but sits closer to calculation results of gaseous phase.

Our new results extend the $\ln^{18}EIE_{H_2O-NO_2^-(aq)}$ values to a wider temperature range than the experimental results. In addition, since the $^{15}\beta$ values of aqueous ammonia and ammonium in our early study (Li et al., 2021) were calculated by the same method, these two sets of data can be directly compared to derive the nitrogen isotope fractionations in the broad $NO_3^- - NO_2^- - NH_4^+ - NH_3$ system. These parameters, combined with the new oxygen isotope data here, provide a robust bonded isotope tool to examine the nitrogen cycle in aqueous systems.

4.4. Inverse isotope effects in nitrite oxidation

It has been demonstrated that nitrate reduction in water column can result in large nitrogen isotope fractionations (−10‰ to −25‰), which is expected to lead to a ^{15}N depletion in nitrite (Granger et al., 2008; Casciotti et al., 2013; Granger and Wankel, 2016). However, the observed $\delta^{15}N$ difference between nitrite and nitrate is larger than expected in suboxic zones (−28‰ to −35‰; Sigman et al., 2003, 2005; Casciotti and McIlvin, 2007). It suggests that there may exist additional mechanisms can result in ^{14}N accumulation in nitrate. Casciotti (2009)

reported an inverse nitrogen isotope effect of +12.9‰ during nitrite oxidation experiments by *Nitrococcus mobilis*, and of +42.9‰ to +51.3‰ based on the calculated vibrational frequencies of nitrate and nitrite at ground state and the estimated zero-point energy of the transition state. The inverse KIE during nitrite oxidation, which is conflict to the common assumption that light isotopes reacts faster in elementary reactions, could lead to the observed strong ^{15}N depletion.

Further studies support such observations (Fig. 6). Buchwald and Casciotti (2010) reported inverse lnKIE_{NO} values of +20.4‰ (±2.5‰) for ^{15}N and +8.2‰ (±2.2‰) for ^{18}O by *Nitrococcus mobilis*, +20.8‰ (±2.8‰) for ^{15}N and +6.5‰ (±1.6‰) for ^{18}O by *Nitrobacter* sp. Nb 355, and +9.2‰ (±1.3‰) for ^{15}N and +1.5‰ (±0.5‰) for ^{18}O by *Nitrospira* marina. More inverse ln$^{15}KIE_{NO}$ values have been also reported for a number of other species, e.g., +31.6‰ (±3.9‰) by *Kuenenia stuttgartiensis* (Brunner et al., 2013), +9.7‰ (±0.8‰) by *Nitrospina watsonii* 347, +10.2‰ (±0.9‰) by *Nitrospina* sp. Ecomares 2.1 (Jacob et al., 2017), +30.6‰ (±3.0‰) by *Ca. Scalindua japonica*, +46.4‰ (±4.2‰) by *Ca. Jettenia caeni*, +32.0‰ (±4.0‰) by *Ca. Brocadia sinica* (Kobayashi et al., 2019), and +9.2‰ (±0.5‰) by *Nitrospina inopinata* (Liu et al., 2021).

So far, studies calibrating the $^{18}KIE_{NO}$ values are relatively few. Incubation experiments using a brackish tidal stream by Boshers et al. (2019) yielded an inverse ln$^{18}KIE_{NO}$ value of +3.9‰ (±0.3‰). The large inverse ^{18}KIE values reported in Kobayashi et al. (2019) are the combined ^{18}KIE values that involve the oxygen introduced from ambient water. In contrast, the $^{18}KIE_{NO}$ values reported in Buchwald and Casciotti (2010), Boshers et al. (2019), and this study are the ^{18}KIE values of NO_2^- alone. Recalculating from Table S1 of Kobayashi et al. (2019), normal ln$^{18}KIE_{NO}$ values of −3.6‰ (±0.7‰), and −3.8‰ (±1.7‰) were obtained by *Ca. Jettenia caeni* and *Ca. Brocadia sinica*, respectively, but an inverse ln$^{18}KIE_{NO}$ value of +6.2‰ (±0.8‰) was obtained by *Ca. Scalindua japonica* (Kobayashi et al., 2019).

The new data in this study provide an opportunity to understand the mechanism for such inverse KIE at molecular level. As mentioned in the Introduction, we can approximate the KIE_{NO} value by $KIE_{NO} \approx \beta_{TS-NapA}/\beta_{NO_2^-}$. Our previous calculation results showed that, at 25 °C, the $\beta_{TS-NapA}$ values are 1.1181 for ^{15}N, and 1.0770 for $^{18}O_{ave}$ (He et al., 2021). The $^{18}KIE_{NO}$ value involves only two oxygens on the nitrogen atom, and therefore the average $^{18}\beta_{TS-NapA}$ value should exclude the oxygen atom on the enzyme. According to Table 5 of He et al. (2021), the average $^{18}\beta_{TS-NapA}$ value for NO process should be 1.0949. Thus, the estimated lnKIE_{NO} values are +15.4‰ for ^{15}N and +5.2‰ for ^{18}O, which verifies inverse kinetic isotope effect occurring for both nitrogen and oxygen during nitrite oxidation.

The ln$^{15}KIE_{NO}$ and ln$^{18}KIE_{NO}$ values determined in this study fall in the range of previous experimental results (Fig. 6). Our calculated ln$^{15}KIE_{NO}$ value is way less than the theoretial estimation by Casciotti (2009). The imaginary frequency estimated from reduced masses and the zero point energy calculated or experimentally determined molecular vibration frequencie were used to predict the ln$^{15}KIE_{NO}$ value of Casciotti (2009). It is understandble that the results may have relatively large uncertainty because the error associated with differnet methods cannot be canceled out during the calculation of ln*EIE* and ln*KIE* values. Thus, Casciotti (2009) only used it as a side supporting evidence for the existence of inverse KIE in their study. Our results were obtained by calculation at the same theoretical level, which is expected to be more accurate. In addition, inverse nitrogen KIE has also been observed in abiotic nitrite oxidation by ligand-bound manganese (III) with ln$^{15}KIE_{NO}$ = +20.1‰ (±0.7‰) (Karolewski et al., 2021). This may imply that such abiotic process might share similar transition state with enzymatic processes. Our calculated ln$^{18}KIE_{NO}$ value shows smaller fractionating magnitude, or less inverse, than the ln$^{15}KIE_{NO}$ value. This is consistent with previous experimental results (Buchwald and Casciotti, 2010; Kobayashi et al., 2019). Normal ln$^{18}KIE_{NO}$ values were only observed in Kobayashi et al. (2019), which should be evaluated carefully.

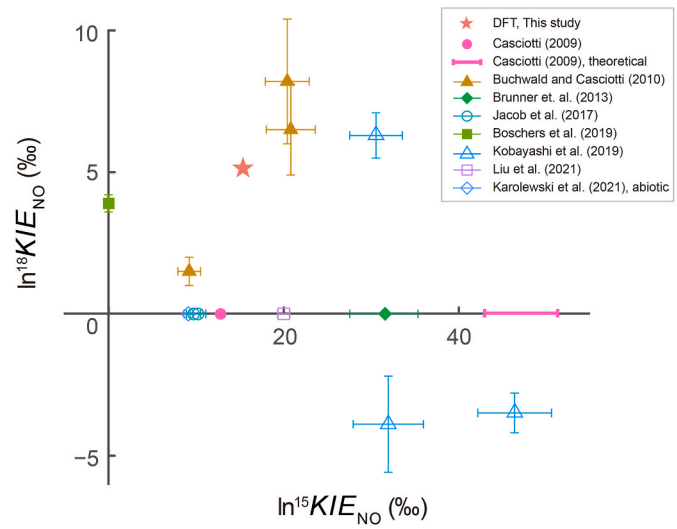

Fig. 6. Comparison of the ln^{18}***KIE*$_{NO}$** − ln^{15}***KIE*$_{NO}$** between this study (red star) and previous incubation experiments unless specified. Detailed descriptions can be found in the Introduction. The results lacking ln^{18}***KIE*$_{NO}$** or ln^{15}***KIE*$_{NO}$** values are put on the axes.

It is expected that the intrinsic KIE values differ from measured isotope fractionation factors. Previously calculated lnKIE_{NR} values are −32.4‰ for ^{15}N, and −20.9‰ for ^{18}O, with ln$^{18}KIE_{NR}$:ln$^{15}KIE_{NR}$ = 0.65 (He et al., 2021), which are consistent with the nitrate reduction experiments using extracted reductase assays (Treibergs and Granger, 2017), but greater than the nitrate reduction experiments using bacterial strains (Granger et al., 2008). The estimated lnKIE_{NO} values differs from bacterial experiments and field observations. These can be attributed to the more complicated processes in laboratory experiments and/or field studies, which can be affected by substrate concentration, microbial activity, commitment to catalysis, transportation across cell membrane, competition between microbial individuals or groups, and/or other mixing or mass transfer processes (He and Bao, 2019; He et al., 2021; Thullner et al., 2012; Treibergs and Granger, 2017). Future nitrite oxidation experiments using extracted reductase assays may test these possibilities.

5. Conclusions

To better estimate the isotope fractionations during the transformation between nitrate and nitrite, we calculate the equilibrium isotope fractionation factors for nitrogen and oxygen in NO_3^-, NO_2^-, and H_2O molecules in gaseous and aqueous phase. The results show that the hybrid-solvent effect has large influences on both β and *EIE* values, which have not been fully assessed in previous studies. The new calculation results provide data to advance our understanding of the nitrogen cycle at low-temperature environments by bonded isotope (i.e., ^{15}N and ^{18}O) effect. The data of this work demonstrate that nitrite oxidation can be associated with inverse kinetic isotope effects of both nitrogen and oxygen that have been previously proposed from laboratory observations.

Declaration of competing interest

The authors declare that they have no known competing financial interests or personal relationships that could have appeared to influence the work reported in this paper.

Acknowledgment

This paper benefitted from valuable discussions with Y.N. Zhang, C. H. Gao, and J. Hayles. The authors thank Y. Liu for providing computational resources. This study is supported by the National Science Foundation of China projects [4217030170, 42150202], the China Postdoctoral Science Foundation [2019M660811], and the pre-research project on Civil Aerospace Technologies of China National Space Administration [D020203].

Appendix A. Supplementary data

Supplementary data to this article can be found online at https://doi.org/10.1016/j.apgeochem.2022.105265.

References

Alhambra, C., Byun, K., Gao, J., 1998. The geometry of water in liquid water from hybrid Ab initio-Monte Carlo and density functional-molecular dynamics simulations. Comb. Quant. Mech. Mol. Mech. Methods. Am. Chem. Soc. 35–49.
Bao, H., Cao, X., Hayles, J.A., 2015. The confines of triple oxygen isotope exponents in elemental and complex mass-dependent processes. Geochem. Cosmochim. Acta 170, 39–50.
Bao, H., Cao, X., Hayles, J.A., 2016. Triple oxygen isotopes: fundamental relationships and applications. Annu. Rev. Earth Planet Sci. 44, 463–492.
Barkan, E., Luz, B., 2005. High precision measurements of 17O/16O and 18O/16O ratios in H2O. Rapid Commun. Mass Spectrom. 19, 3737–3742.
Becke, A.D., 1993. Density-functional thermochemistry. III. The role of exact exchange. J. Chem. Phys. 98, 5648–5652.
Begun, G.M., Fletcher, W.H., 1960. Partition function ratios for molecules containing nitrogen isotopes. J. Chem. Phys. 33, 1083–1085.
Bigeleisen, J., 1949. The relative reaction velocities of isotopic molecules. J. Chem. Phys. 17, 675–678.
Bigeleisen, J., Goeppert Mayer, M., 1947. Calculation of equilibrium constants for isotopic exchange reactions. J. Chem. Phys. 15, 261–267.
Böhlke, J.K., Mroczkowski, S.J., Coplen, T.B., 2003. Oxygen isotopes in nitrate: new reference materials for 18O:17O:16O measurements and observations on nitrate-water equilibration. Rapid Commun. Mass Spectrom. 17, 1835–1846.
Boshers, D.S., Granger, J., Tobias, C.R., Böhlke, J.K., Smith, R.L., 2019. Constraining the oxygen isotopic composition of nitrate produced by nitrification. Environ. Sci. Technol. 53 (3), 1206–1216. https://doi.org/10.1021/acs.est.8b03386. Epub 2019 Jan 22. PMID: 30605314.
Bottinga, Y., 1968. Calculation of fractionation factors for carbon and oxygen isotopic exchange in the system calcite-carbon dioxide-water. J. Phys. Chem. 72, 800–808.
Boxe, C.S., Colussi, A.J., Hoffmann, M.R., Perez, I.M., Murphy, J.G., Cohen, R.C., 2006. Kinetics of NO and NO2 evolution from illuminated frozen nitrate solutions. J. Phys. Chem. 110, 3578–3583.
Brunner, B., Contreras, S., Lehmann, M.F., Matantseva, O., Rollog, M., Kalvelage, T., Klockgether, G., Lavik, G., Jetten, M.S.M., Kartal, B., Kuypers, M.M.M., 2013. Nitrogen isotope effects induced by anammox bacteria. Proc. Natl. Acad. Sci. Unit. States Am. 110, 18994–18999.
Buchwald, C., Casciotti, K.L., 2010. Oxygen isotopic fractionation and exchange during bacterial nitrite oxidation. Limnol. Oceanogr. 55 (3), 1064–1074.
Buchwald, C., Casciotti, K.L., 2013. Isotopic ratios of nitrite as tracers of the sources and age of oceanic nitrite. Nat. Geosci. 6, 308–313.
Casciotti, K.L., Bohlke, J.K., McIlvin, M.R., Mroczkowski, S.J., Hannon, J.E., 2007. Oxygen isotopes in nitrite: analysis, calibration, and equilibration. Anal. Chem. 79, 2427–2436.
Casciotti, K., McIlvin, M., 2007. Isotopic analyses of nitrate and nitrite from reference mixtures and application to Eastern Tropical North Pacific waters. Mar. Chem. 107, 184–201.
Casciotti, K.L., 2009. Inverse kinetic isotope fractionation during bacterial nitrite oxidation. Geochem. Cosmochim. Acta 73, 2061–2076.
Casciotti, K.L., Buchwald, C., McIlvin, M., 2013. Implications of nitrate and nitrite isotopic measurements for the mechanisms of nitrogen cycling in the Peru oxygen deficient zone. Deep-Sea Res. Pt I 80, 78–93.
Cerqueira, N.M.F.S.A., Gonzalez, P.J., Brondino, C.D., Romao, M.J., Romao, C.C., Moura, I., Moura, J.J.G., 2009. The effect of the sixth sulfur ligand in the catalytic mechanism of periplasmic nitrate reductase. J. Comput. Chem. 30, 2466–2484.
Cerqueira, N.M.F.S.A., Pakhira, B., Sarkar, S., 2015. Theoretical studies on mechanisms of some Mo enzymes. J. Biol. Inorg. Chem. 20, 323–335.
Császár, A.G., Czakó, G., Furtenbacher, T., Tennyson, J., Szalay, V., Shirin, S.V., Zobov, N.F., Polyansky, O.L., 2005. On equilibrium structures of the water molecule. J. Chem. Phys. 122, 214305.
Dore, J.E., Karl, D.M., 1996. Nitrification in the euphotic zone as a source for nitrite, nitrate, and nitrous oxide at Station ALOHA. Limnol. Oceanogr. 41, 1619–1628.
Fanourgakis, G.S., Xantheas, S.S., 2006a. The bend angle of water in ice Ih and liquid water: the significance of implementing the nonlinear monomer dipole moment surface in classical interaction potentials. J. Chem. Phys. 124, 174504.
Fanourgakis, G.S., Xantheas, S.S., 2006b. The flexible, polarizable, Thole-type interaction potential for water (TTM2-F) revisited. J. Phys. Chem. 110, 4100–4106.
Frisch, M.J., Pople, J.A., Binkley, J.S., 1984. Self-consistent molecular orbital methods 25. Supplementary functions for Gaussian basis sets. J. Chem. Phys. 80, 3265–3269.
Frisch, M.J., Trucks, G.W., Schlegel, H.B., Scuseria, G.E., Robb, M.A., Cheeseman, J.R., Scalmani, G., Barone, V., Petersson, G.A., Nakatsuji, H., Li, X., Caricato, M., Marenich, A.V., Bloino, J., Janesko, B.G., Gomperts, R., Mennucci, B., Hratchian, H. P., Ortiz, J.V., Izmaylov, A.F., Sonnenberg, J.L., Williams, Ding, F., Lipparini, F., Egidi, F., Goings, J., Peng, B., Petrone, A., Henderson, T., Ranasinghe, D., Zakrzewski, V.G., Gao, J., Rega, N., Zheng, G., Liang, W., Hada, M., Ehara, M., Toyota, K., Fukuda, R., Hasegawa, J., Ishida, M., Nakajima, T., Honda, Y., Kitao, O., Nakai, H., Vreven, T., Throssell, K., Montgomery Jr., J.A., Peralta, J.E., Ogliaro, F., Bearpark, M.J., Heyd, J.J., Brothers, E.N., Kudin, K.N., Staroverov, V.N., Keith, T.A., Kobayashi, R., Normand, J., Raghavachari, K., Rendell, A.P., Burant, J.C., Iyengar, S. S., Tomasi, J., Cossi, M., Millam, J.M., Klene, M., Adamo, C., Cammi, R., Ochterski, J. W., Martin, R.L., Morokuma, K., Farkas, O., Foresman, J.B., Fox, D.J., 2016. Gaussian 16 Rev. C.01. 2016.
Gao, C., Cao, X., Liu, Q., Yang, Y., Zhang, S., He, Y., Tang, M., Liu, Y., 2018. Theoretical calculation of equilibrium Mg isotope fractionations between minerals and aqueous solutions. Chem. Geol. 488, 62–75.
Granger, J., Sigman, D.M., Lehmann, M.F., Tortell, P.D., 2008. Nitrogen and oxygen isotope fractionation during dissimilatory nitrate reduction by denitrifying bacteria. Limnol. Oceanogr. 53, 2533–2545.
Granger, J., Wankel, S.D., 2016. Isotopic overprinting of nitrification on denitrification as a ubiquitous and unifying feature of environmental nitrogen cycling. Proc. Natl. Acad. Sci. U.S.A. 113, E6391–E6400.
Hayles, J., Gao, C., Cao, X., Liu, Y., Bao, H., 2018. Theoretical calibration of the triple oxygen isotope thermometer. Geochem. Cosmochim. Acta 235, 237–245.
He, Y., Bao, H., 2019. Predicting high-dimensional isotope relationships from diagnostic fractionation factors in systems with diffusional mass transfer. ACS Earth Space Chem. 3, 120–128.
He, Y., Bao, H., Liu, Y., 2020a. Predicting equilibrium intramolecular isotope distribution within a large organic molecule by the cutoff calculation. Geochem. Cosmochim. Acta 269, 292–302.
He, Y., Cao, X., Bao, H., 2020b. Ideas and perspectives: the same carbon behaves like different elements – an insight into position-specific isotope distributions. Biogeosciences 17, 4785–4795.
He, Y., Zhang, Y., Zhang, S., Liu, Y., 2021. Predicting nitrogen and oxygen kinetic isotope effects of nitrate reduction by periplasmic dissimilatory nitrate reductase. Geochem. Cosmochim. Acta 293, 224–239.
Hille, R., 1996. The mononuclear molybdenum enzymes. Chem. Rev. 96, 2757–2816.
Hille, R., 2002. Molybdenum and tungsten in biology. Trends Biochem. Sci. 27, 360–367.
Horita, J., Wesolowski, D.J., 1994. Liquid-vapor fractionation of oxygen and hydrogen isotopes of water from the freezing to the critical-temperature. Geochem. Cosmochim. Acta 58, 3425–3437.
Ichikawa, K., Kameda, Y., Yamaguchi, T., Wakita, H., Misawa, M., 1991. Neutron-diffraction investigation of the intramolecular structure of a water molecule in the liquid phase at high temperatures. Mol. Phys. 73, 79–86.
Jacob, J., Nowka, B., Merten, V., Sanders, T., Spieky, E., Dähnke, K., 2017. Oxidation kinetics and inverse isotope effect of marine nitrite-oxidizing isolates. Aquat. Microb. Ecol. 80, 289–300.
Jones, J.P., Urbauer, J.L., 1991. Theoretical kinetic isotope effects for the hydride transfer from formate to carbon dioxide: a comparison of theory with experiment. J. Comput. Chem. 12, 1134–1141.
Kobayashi, K., Makabe, A., Yano, M., Oshiki, M., Kindaichi, T., Casciotti, K.L., Okabe, S., 2019. Dual Nitrogen and Oxygen Isotope Fractionation during Anaerobic Ammononium Oxidation by Anammox Bacteria, 13, pp. 2426–2436.
Karolewski, J.S., Sutherland, K.M., Hansel, C.M., Wankel, S.D., 2021. An isotopic study of abiotic nitrite oxidation by ligand-bound manganese (III). Geochem. Cosmochim. Acta 293, 365–378.
Lee, C., Yang, W., Parr, R.G., 1988. Development of the Colle-Salvetti correlation-energy formula into a functional of the electron density. Phys. Rev. B 37, 785.
Li, L., He, Y., Zhang, Z., Liu, Y., 2021. Nitrogen isotope fractionations among gaseous and aqueous NH4+, NH3, N2, and metal-ammine complexes: theoretical calculations and applications. Geochem. Cosmochim. Acta 295, 80–97.
Lipschultz, F., Zafiriou, O.C., Ball, L.A., 1996. Seasonal fluctuations of nitrite concentrations in the deep oligotrophic ocean. Deep-Sea Res Pt II 43, 403–419.
Liu, Q., Tossell, J.A., Liu, Y., 2010. On the proper use of the Bigeleisen–Mayer equation and corrections to it in the calculation of isotopic fractionation equilibrium constants. Geochem. Cosmochim. Acta 74, 6965–6983.
Liu, S., Jung, M.-Y., Zhang, S., Wagner, M., Daims, H., Wanek, W., 2021. Nitrogen kinetic isotope effects of nitrification by the complete ammonia oxidizer Nitrospira inopinata. mSphere 6 (6) e00634-21.
Majoube, M., 1971. Fractionnement en oxygène 18 et en deutérium entre l'eau et sa vapeur. J. Chim. Phys. 68, 1423–1436.
Megyes, T., Bálint, S., Peter, E., Grósz, T., Bakó, I., Krienke, H., Bellissent-Funel, M.-C., 2009. Solution structure of NaNO3 in water: diffraction and molecular dynamics simulation study. J. Phys. Chem. B 113, 4054–4064.
Méheut, M., Lazzeri, M., Balan, E., Mauri, F., 2007. Equilibrium isotopic fractionation in the kaolinite, quartz, water system: prediction from first-principles density-functional theory. Geochem. Cosmochim. Acta 71, 3170–3181.
Meincke, M., Bock, E., Kastrau, D., Kroneck, P.M.H., 1992. Nitrite oxidoreductase from Nitrobacter hamburgensis: redox centers and their catalytic role. Arch. Microbiol. 158, 127–131.
Monse, E.U., Spindel, W., Stern, M.J., 1969. Analysis of isotope-effect calculations illustrated with exchange equilibria among oxynitrogen compounds. Isotope Effects Chem. Process. Am. Chem. Soc. 148–184.

Narten, A.H., Levy, H.A., 1971. Liquid water: molecular correlation functions from X-ray diffraction. J. Chem. Phys. 55, 2263–2269.
Niks, D., Hille, R., 2019. Molybdenum- and tungsten-containing formate dehydrogenases and formylmethanofuran dehydrogenases: structure, mechanism, and cofactor insertion. Protein Sci 28, 111–122.
Petts, D., Chacko, T., Stachel, T., Stern, R., Heaman, L., 2015. A nitrogen isotope fractionation factor between diamond and its parental fluid derived from detailed SIMS analysis of a gem diamond and theoretical calculations. Chem. Geol. 410, 188–200.
Powles, J.G., 1981. The structure of the water molecule in liquid water. Mol. Phys. 42, 757–765.
Richet, P., Bottinga, Y., Javoy, M., 1977. A review of hydrogen, carbon, nitrogen, oxygen, sulphur, and chlorine stable isotope fractionation among gaseous molecules. Annu. Rev. Earth Planet Sci. 5, 65–110.
Rustad, J.R., Casey, W.H., Yin, Q.-Z., Bylaska, E.J., Felmy, A.R., Bogatko, S.A., Jackson, V.E., Dixon, D.A., 2010. Isotopic fractionation of Mg2+(aq), Ca2+(aq), and Fe2+(aq) with carbonate minerals. Geochem. Cosmochim. Acta 74, 6301–6323.
Rustad, J.R., Nelmes, S.L., Jackson, V.E., Dixon, D.A., 2008. Quantum-chemical calculations of carbon-isotope fractionation in CO2 (g., aqueous carbonate species, and carbonate minerals. J. Phys. Chem. 112, 542–555.
Saxena, S.C., Bhatnagar, D.N., Ramaswamy, S., 1962. Partition function ratios and equilibrium constants for oxygen-18 exchange reactions. J. Chem. Eng. Data 7, 240–242.
Scalmani, G., Frisch, M.J., 2010. Continuous surface charge polarizable continuum models of solvation. I. General formalism. J. Chem. Phys. 132.
Schauble, E.A., Ghosh, P., Eiler, J.M., 2006. Preferential formation of 13C–18O bonds in carbonate minerals, estimated using first-principles lattice dynamics. Geochem. Cosmochim. Acta 70, 2510–2529.
Sigman, D.M., Granger, J., DiFiore, P.J., Lehmann, M.M., Ho, R., Cane, G., van Geen, A., 2005. Coupled nitrogen and oxygen isotope measurements of nitrate along the eastern North Pacific margin. Global Biogeochem. Cycles 19.
Sigman, D.M., Robinson, R., Knapp, A.N., van Geen, A., McCorkle, D.C., Brandes, J.A., Thunell, R.C., 2003. Distinguishing between water column and sedimentary denitrification in the Santa Barbara Basin using the stable isotopes of nitrate. G-cubed 4.
Silvestrelli, P.L., Parrinello, M., 1999. Structural, electronic, and bonding properties of liquid water from first principles. J. Chem. Phys. 111, 3572–3580.
Sparacino-Watkins, C., Stolz, J.F., Basu, P., 2014. Nitrate and periplasmic nitrate reductases. Chem. Soc. Rev. 43, 676–706.
Spieck, E., Ehrich, S., Aamand, J., Bock, E., 1998. Isolation and immunocytochemical location of the nitrite-oxidizing system in Nitrospira moscoviensis. Arch. Microbiol. 169, 225–230.
Spindel, W., 1954. The calculation of equilibrium constants for several exchange reactions of nitrogen-15 between oxy compounds of nitrogen. J. Chem. Phys. 22, 1271–1272.
Stern, M.J., Kauder, L.N., Spindel, W., 1962. Isotopic fractionation of nitrogen in the nitrogen oxide-nitrate exchange system. J. Chem. Phys. 36, 764–772.
Thornton, E.R., 1962. Solvent isotope effects in H2O16 and H2O18. J. Am. Chem. Soc. 84, 2474–2475.
Thullner, M., Centler, F., Richnow, H.-H., Fischer, A., 2012. Quantification of organic pollutant degradation in contaminated aquifers using compound specific stable isotope analysis - review of recent developments. Org. Geochem. 42, 1440–1460.
Treibergs, L.A., Granger, J., 2017. Enzyme level N and O isotope effects of assimilatory and dissimilatory nitrate reduction. Limnol. Oceanogr. 62, 272–288.
Urey, H.C., 1947. The thermodynamic properties of isotopic substances. J. Chem. Soc. 562–581.
Vchirawongkwin, V., Kritayakornupong, C., Tongraar, A., Rode, B.M., 2011. Symmetry breaking and hydration structure of carbonate and nitrate in aqueous solutions: a study by Ab initio quantum mechanical charge field molecular dynamics. J. Phys. Chem. B 115, 12527–12536.
Walford, G., Clarke, J.H., Dore, J.C., 1977. The structure of the heavy water molecule from neutron-diffraction measurements. Mol. Phys. 33, 25–30.
Walters, W.W., Michalski, G., 2015. Theoretical calculation of nitrogen isotope equilibrium exchange fractionation factors for various NOy molecules. Geochem. Cosmochim. Acta 164, 284–297.
Walters, W.W., Michalski, G., 2016. Theoretical calculation of oxygen equilibrium isotope fractionation factors involving various NOy molecules, OH, and H2O and its implications for isotope variations in atmospheric nitrate. Geochem. Cosmochim. Acta 191, 89–101.
Wang, H.-W., Vlcek, L., Neuefeind, J.C., Page, K., Irle, S., Simonson, J.M., Stack, A.G., 2018. Decoding oxyanion aqueous solvation structure: a potassium nitrate example at saturation. J. Phys. Chem. B 122, 7584–7589.
Wankel, S.D., Buchwald, C., Ziebis, W., Wenk, C.B., Lehmann, M.F., 2015. Nitrogen cycling in the deep sedimentary biosphere: nitrate isotopes in porewaters underlying the oligotrophic North Atlantic. Biogeosciences 12, 7483–7502.
Wei, X., Peng, Q., Ding, J., Yang, X., Yang, J., Long, B., 2013. Theoretical study on thermal stability of molten salt for solar thermal power. Appl. Therm. Eng. 54, 140–144.
Xantheas, S.S., 1995. Ab initio studies of cyclic water clusters, H2O.n, n=1–6. III. Comparison of density functional with MP2 results. J. Chem. Phys. 102, 4505–4517.
Zeebe, R.E., 2020. Oxygen isotope fractionation between water and the aqueous hydroxide ion. Geochem. Cosmochim. Acta 289, 182–195.
Zhang, S.T., Liu, Y., 2014. Molecular-level mechanisms of quartz dissolution under neutral and alkaline conditions in the presence of electrolytes. Geochem. J. 48, 189–205.